

# Study of the isotropic contribution to the analysis of photoelectron diffraction experiments at the ALOISA beamline

F. Bruno<sup>a</sup>, L. Floreano<sup>a,\*</sup>, A. Verdini<sup>a</sup>, D. Cvetko<sup>a,b</sup>, R. Gotter<sup>a</sup>, A. Morgante<sup>a,c</sup>.

<sup>a</sup>Laboratorio TASC dell'Istituto Nazionale per la Fisica della Materia, S.S.14 Km 163.5, Basovizza, 34012 Trieste, Italy

<sup>b</sup>J. Stefan Institute, University of Ljubljana, Slovenia, and Sincrotrone Trieste, Italy.

<sup>c</sup>Dipartimento di Fisica dell'Università di Trieste, Italy.

M. Canepa, S.Terreni

INFN and Dipartimento di Fisica dell'Università di Genova, Italy.

The angular distribution of the intensity in photoemission experiments is affected by electron diffraction patterns and by a smoothly varying contribution originated by both instrumental details and physical properties of the samples. The peculiar variety of scattering configurations available at the ALOISA beamline experimental station in Trieste stimulated the development of an analytical description for the smooth angular dependence sustaining the diffraction features. We present here the basic formulae and their application to experimental data taken on the Fe/Cu<sub>3</sub>Au(001) system in order to highlight the role of the various parameters included in the distribution function. A specific model for the surface illumination has been developed as well as the overlayer thickness and surface roughness have been considered.

*Keywords:* Angular resolved photoemission; Photoelectron diffraction; Thin films.

\* \* Corresponding author: Fax: +39-04-226767, *E-mail address:* floreano@tasc.infn.it

## I. INTRODUCTION

The study of the angular distribution of the Auger- and photo-electrons at medium kinetic energies (a few hundreds of eV) is a well established method to determine the atomic structure in a local environment surrounding the emitting atoms close to the surface of ordered materials. The lattice geometry is usually retrieved exploiting the observation of intensity maxima along the direction of close packed atom rows. By taking into account the electron diffraction (ED) features, one can also reconstruct the atomic distances between the emitter and its closest neighbors.

In general, the distribution of the intensity in the ED patterns is originated by two contributions: one anisotropic component  $\chi$ , which is determined by the geometry of the local atomic structure, and one, slowly varying, isotropic component *ISO* which depends from both instrumental factors (such as sample illumination and detector angular resolution) and material dependent factors (such as atomic differential cross section, film thickness/escape depth, surface morphology/roughness).

The origin of the various contributions to the *ISO* component has been identified since many years [1–3]. Some aspects relevant to photoelectron diffraction have been recently reviewed [4], in particular regarding the role of dipolar emission in surface science experiments. Nonetheless in this work we present original development of the ED analysis, which arises from the evolution of instrumental performance, in terms of analyzers positioning and angular resolution, as well as collimation and size of X-ray beams in third generation synchrotron sources. The analytical treatment of the instrumental factors is presented in detail for the end station of the ALOISA beamline (Trieste Synchrotron), where a wide variety of scattering geometries is available for ED experiments.

In the following, we present a functional form of the *ISO* component using physically meaningful parameters, that can be fitted at once with the  $\chi$  component to rigorously deal with the ED analysis. This functional form has been coupled to multiple scattering calculations of the anisotropic structure-dependent  $\chi$  component (we made use of the MSCD code by Chen and Van Hove [5]). This fitting procedure was applied to the structural study of thin Fe films grown on the Cu<sub>3</sub>Au(001) surface, where the Fe structure changes from an fcc-like configuration to a bcc-like one as a function of the film thickness. [6,7] For this system, Auger- and photo-electron ED data were taken in combination with in-plane X-ray diffraction. [8] The latter technique yielded the lateral lattice parameter of the growing film with utmost precision and its value was used as input in the fitting of the ED patterns, the vertical lattice spacing thus being the only structural parameter to be determined. In the next section, we have compared our model of the *ISO* function with the ED data taken for a few Fe films to enlight the weight of a proper choice of the *ISO* functional form in the determination of the  $\chi$  component.

## II. EXPERIMENTAL SETUP

The experimental chamber of the ALOISA beamline hosts several electron and photon detectors in UHV for the study of surface photoemission, X-ray and photoelectron diffraction. This experimental setup exploits the very wide photon energy range given by the ALOISA grating-crystal monochromator, which spans from the dominion of X-ray photoemission spectroscopy (hundreds of eV) to that of X-ray diffraction (thousands of eV) [9]. The three angular degrees of freedom given by the manipulator (a modified CTPO manipulator by Vacuum Generators) allow one to freely orient the sample surface with respect to the photon beam direction and the beam linear polarization. At the same time, the combined rotation of the frame (rotation *B*) hosting in UHV the electron analyzers, and of the whole experimental chamber (rotation *C*) allows one to explore a wide portion of the hemisphere above the surface for any sample orientation. (see Fig. 1 for a sketch of the scattering geometries accessible by the detectors). The electron analyzers are of the hemispherical type with a 33 mm mean radius and an optical lens system yielding an acceptance angle of  $\sim 1^\circ$  (FWHM) and a field of view of  $\sim 1 \times 4 \text{ mm}^2$  [10]. The transverse size (FWHM) of the photon beam at the sample position is  $\sim 20 \mu\text{m}$  vertically and  $\sim 150 \mu\text{m}$  horizontally, with a slight dependence on the photon energy. The photon beam is linearly polarized, with the electric field vector  $\vec{E}$  in the horizontal plane [11].

ED polar scans are usually collected by rotating one electron analyzer in the scattering plane from the surface normal to the horizon (polar angle  $\theta$ ), even though different geometries can be suitable to specific experimental requirements, such as photoelectron holography [12] or near node photoelectron diffraction [13]. As far as the data reported in this paper are concerned, the scans have been taken in transverse-magnetic polarization with the substrate [001] direction oriented along the photon beam direction for a few selected grazing angles  $\alpha$  on the surface. In the present case, the ED patterns have been collected for the Fe L<sub>23</sub>M<sub>23</sub>M<sub>45</sub> Auger line at a kinetic energy of 698 eV (we used a photon energy of 900 eV). In one case, we measured the ED pattern from a polycrystalline Fe sample for the 3p core level at a kinetic energy of 803 eV. The signal was always taken at the maximum of the corresponding spectral line and at

two suitably chosen energies aside the peak, in order to allow an effective subtraction of the background of secondary electrons. The films were prepared by in situ evaporation of Fe on a Cu<sub>3</sub>Au(001) surface and the thickness was measured in situ by X-ray reflectivity (further detail about the sample preparation can be found elsewhere [8]). After an initial pseudomorphic stage, the Fe films assume a tetragonally distorted bcc structure, displaying a (001) surface orientation, but rotated by 45° with respect to the substrate. At the largest thickness considered here (36 Å), the Fe film has almost recovered its bcc bulk structure, with a lateral lattice spacing  $a = 2.830 \pm 0.005$  Å, as measured by in-plane X-ray diffraction [8].

### III. DESCRIPTION OF THE *ISO* FUNCTION

*a. Angles definition* A schematic picture of the angular degrees of freedom available in the determination of the scattering geometry is shown in Fig.1. The manipulator rotation  $\phi$  is used to select the azimuthal orientation of the surface, without altering the grazing angle which is selected by the rotation  $\alpha$ . The surface normal can be rotated around the beam axis by  $\pm 180^\circ$  with the manipulator rotation  $\xi$ : at  $\xi = 0^\circ$  the surface normal vector  $\hat{n}$  lies in the plane normal to the electric field vector  $\vec{E}$ .

The rotation  $B$  of the electron analyzer frame sets the deflection angle between the X-ray beam and the photoelectron wavevector  $\vec{k}$ , with a clearance of  $\pm 115^\circ$ . Furthermore, the frame rotation axis  $\hat{B}$  can be oriented in the  $y-z$  plane of the laboratory reference system exploiting the  $C$  rotation of the whole experimental chamber (independently of the manipulator settings). In particular,  $\hat{B}$  is related to the rotation  $C$  as  $\hat{B} = \hat{z} \cos C - \hat{y} \sin C$ .

According to these definitions, the polar emission angle  $\theta$  (defined by  $\vec{k}$  and the surface normal direction  $\hat{n}$ ) is defined as:

$$\cos \theta(\xi, \alpha, B, C) = -\cos B \sin \alpha + \sin B \cos C \cos \alpha \sin \xi + \sin B \sin C \cos \alpha \cos \xi, \quad (1)$$

which simplifies to  $\theta = 90^\circ - (B - \alpha)$  if the analyzer is rotated in the plane containing the surface normal, which is often the case if the projection of the photoelectron wavevector onto the surface plane is to be maintained along a specific azimuthal direction, as in ED polar scans.

In the following we describe the factors contributing to the measured *ISO* electron yield.

*b. Atomic cross-section* In the dipole approximation (we will not consider multipolar expansion coefficients in the following applications), the atomic differential cross-section  $d\sigma_{nl}/d\Omega$  for the  $nl$  initial state of the photoemission process takes the well known analytical expression,

$$\frac{d\sigma_{nl}}{d\Omega}(\beta; \gamma) \propto [1 + \frac{1}{2}\beta(3 \cos^2 \gamma - 1)], \quad (2)$$

where  $\beta(nl, h\nu)$  is the asymmetry parameter in the matrix elements for the photoemission process [14] and  $\gamma$  is the angle between the directions of the polarization vector  $\vec{E}$  and the photoelectron wavevector  $\vec{k}$  (see Fig.1). The value of  $\cos \gamma = \sin B \cos C$  is determined only by the  $B$  and  $C$  rotations of the electron analyzer, independently from the sample surface orientation.

*c. Escape depth* The effect of inelastic scattering on the probability of escape of photoelectrons from the surface of condensed matter samples is described by means of the inelastic mean free path (IMFP), whose variation as a function of the electron kinetic energy is well known and can be evaluated by analytical formulas [15].

The flux of electrons emitted at a depth  $z$  and detected at a polar angle  $\theta$  from the surface normal will be reduced by inelastic scattering according to the Beer-Lambert relationship  $I(z, \theta) = e^{-\frac{z}{\lambda \cos \theta}}$ .

Integration over the depth from the surface yields the angular dependence expected for an emitting slab of matter of thickness  $D$

$$I_{IMFP}(D, \lambda; \theta) = \int_0^D I(z, \theta) dz = \lambda \cos \theta [1 - e^{-\frac{D}{\lambda \cos \theta}}] \quad (3)$$

which corresponds to the well known  $\sim \cos(\theta)$  behaviour in the limit  $D \rightarrow \infty$  of an homogeneous semi-infinite emitting volume.

The same description can be used to describe the reduction of the photoemission intensity caused by a non-emitting layer, i.e. with different chemical composition, above the emitting region of the sample. Considering an emitting layer of thickness  $D$  below a non-emitting one of thickness  $D'$ , the full formula can be written as:

$$I_{IMFP}(D, \lambda, D', \lambda'; \theta) = \lambda \cos \theta [1 - e^{-\frac{D}{\lambda \cos \theta}}] e^{-\frac{D'}{\lambda' \cos \theta}} \quad (4)$$

Further, the limited penetration of the X-ray beam can be taken into account: this yields a very small correction, since the IMFP of the photoelectrons at the kinetic energies typical of photoemission experiments (50-1000 eV) is of the order of 10 Å, while the characteristic penetration depth of the X-ray photons is normally larger than 50 Å.

*d. Surface roughness* The angular distribution of the photoelectron intensity, specially for high values of polar angle, is also affected by the surface roughness of the emitting layer. Models can be set up, to take into account the effects of shadowing of the photoelectron flux at grazing emission, where the details of the resulting formulae depend on the details of the surface morphology [3].

A simple statistical model, which can be used in a phenomenological way, has been described in Ref. [16]. The rough surface is described in terms of an isotropic stationary random function  $z(x, y)$  of the in-plane surface coordinates with a mean value  $\langle z \rangle = 0$ . The distribution of heights is assumed to be normal, so that the probability density for  $z$  is  $f(z) = \frac{1}{\sqrt{2\pi}\sigma} e^{-\frac{z^2}{2\sigma^2}}$ .

After a statistical analysis of the average shadowing by the surface protrusions, an analytical expression  $I_R(\delta, \theta)$  for the dependence on the polar angle  $\theta$  is derived. Details of the formulae can be found in Ref. [16]. Qualitatively speaking,  $I_R$  assumes a constant unit value near normal emission, and drops to zero for  $\theta \rightarrow 90^\circ$ , the steepness of the decay being determined by the amount of surface roughness. The shadowing can be completely neglected up to a maximum take-off value of the polar angle  $\arctan(\delta)$ , so that the phenomenological parameter  $\delta$  can be used as an effective marker of the surface roughness.

*e. Surface illumination* Due to the high angular resolution of the ALOISA analyzers (acceptance angle of  $1^\circ$ , FWHM), the angular smearing of the *ISO* function originated by the angular acceptance can be neglected, although it must be taken into consideration in the simulation of the ED pattern  $\chi$ . On the other hand, the interplay between the size of the field of view and the illuminated portion area of the surface must be carefully taken into account. All the experiments at ALOISA are performed at grazing incidence, i.e. the value of the grazing angle  $\alpha$  of the photon beam with respect to the sample surface is always in the  $[0 - 10^\circ]$  range. Further,  $\alpha$  is often set to values as low as a few degrees in order to exploit the increase of the signal from the surface region when total reflection condition are satisfied. Even if the transverse width  $\Gamma_{beam}$  of the focussed photon beam (FWHM) is narrow, the beam footprint on the surface is elongated in the beam direction. The width of the illuminated surface area  $\Gamma(\alpha) = \Gamma_{beam}/\sin\alpha$  can easily exceed the width of the surface area representing the projection of the analyzer slits ( $1 \times 4mm^2$ ), specially when working in very grazing conditions ( $\alpha_{in} \sim 1^\circ$ ) and in transverse magnetic polarization,  $\xi = 90^\circ$ , where  $\Gamma_{beam}$  has its maximum value of  $\sim 150 \mu m$ . This polarization setting is indeed the most frequently used, since it takes the nodal planes of the atomic cross-section close to the surface horizon.

The beam footprint on the surface can be considered as an unidimensional Gaussian intensity distribution  $exp\left\{-\frac{x^2}{2\Gamma^2(\alpha)}\right\}$  (see Fig. 2), since the transverse distribution is always completely integrated by the analyzer slits.

The integration of the photoemission intensity over the portion of illuminated area of the sample surface then results in the intensity factor

$$I_{ILL}(\Gamma_{beam}, \alpha; B, C) = \int_{-L/2}^{L/2} exp\left\{-\frac{x^2}{2(\Gamma(\alpha)/2.35)^2}\right\} dx \quad (5)$$

The width  $L$  of the portion of illuminated area, which overlaps to the projected area of the analyzer slits onto the sample surface, can be derived analytically, for any orientation of the sample surface and detector position. For a generic scattering configuration,  $L$  is a non-trivial function of the experimental angles  $B, C, \xi$  and  $\alpha$ , and can be also limited by the finite sample size. The complete description of the general case is given in the Appendix. For simple polar scans, in which the analyzer is rotated in the scattering plane defined by the photon wavevector and the surface normal,  $L$  takes the minimum value between the sample size and the projected slit width on the surface  $\Delta/\cos\theta$ . (see Fig. 2)

*f. Complete ISO formula* The complete formula combines all the described factors:

$$ISO = A \cdot \frac{d\sigma_{nl}}{d\Omega}(\beta) \cdot I_{IMFP}(D/\lambda, D'/\lambda') \cdot I_R(\delta) \cdot I_{ILL}(\Gamma_{beam}, \alpha), \quad (6)$$

where, for the sake of clarity, only the fitting parameters have been explicitly reported in the arguments of each correction factor. The cross-section asymmetry parameter  $\beta$  and the IMFP  $\lambda, \lambda'$  are set to calculated values.  $A$  is a scale factor to be determined by fitting the data as well as the roughness parameter  $\delta$ . The X-ray beam width  $\Gamma_{beam}$  and the grazing angle  $\alpha$  are usually set to the nominal values in the first step of the iterative fitting procedure. The emitting layer thickness  $D$  and the non-emitting overlayer thickness  $D'$  are also used as fitting parameters, unless an independent measurement is available for them (for instance by means of X-ray specular reflectivity [8]).

#### IV. DATA ANALYSIS

In Fig. 3 a series of polar scans of the Fe Auger LMM line taken for a few Fe films on Cu<sub>3</sub>Au(001) are shown. For each film thickness, the experimental curve is compared with the calculated *ISO* distribution.

In order to emphasize the dependence on the emitting thickness  $D$  (see Eq. 3), the curves were divided by a  $\cos\theta$  factor. Besides the structural transition from fcc(100) to bcc(100) $R45^\circ$  (witnessed by the angular shift of the main forward focusing directions), the weight of the thickness of the emitting layer on the *ISO* shape is remarkable, particularly at the highest values of polar emission. The calculations were performed using the nominal Fe overlayer thicknesses (as determined by X-ray reflectivity) and an IMFP of 13.4 Å. The roughness parameter  $\delta$  was used as a free parameter and adjusted with a minimization procedure to the experimental data. For all the considered thicknesses, it fell in the range  $\delta = 1.0 \pm 0.1$  (maximum un-shadowed takeoff angle  $\sim 45^\circ$ ).

To enlight the role of the illumination correction factor we show here data taken from the surface of a polycrystalline Fe sample, where the anisotropy  $\chi$  component is absent and the ED pattern can be simply reproduced by the *ISO* component. The polar scans of the Fe 3p photoelectron intensity (taken at a kinetic energy of 803 eV) are shown in Fig. 4 in comparison to a few calculated *ISO* functions, built by successive inclusion of inelastic scattering, atomic cross-section and illumination correction factors. The complete *ISO* component accurately fits the experimental data with the same set of parameters for both the scans. The illumination factor  $I_{ILL}$  was calculated using  $\Gamma_{beam} = 150 \mu\text{m}$  and  $\alpha$  set to the nominal values, as indicated in the Figure. The asymmetry parameter in the cross-section factor was set to  $\beta = 1.485$ , as calculated using one of the standard formulae [15]. As expected, the weight of the illumination factor on the *ISO* function is more significant at lower grazing angles. Small values of the grazing angle  $\alpha$  are usually chosen in the experiment settings in order to exploit the enhancement of the surface signal, obtained when  $\alpha$  is as small as the critical value for total external reflection (of the order of a few degrees for soft X-rays).

As far as the structural analysis is concerned, the  $\chi$  component is often extracted by subtracting an *ISO* component, as obtained by interpolation of the ED pattern with a polynomial or a cosine function. The comparison between the so obtained experimental anisotropy and simulations based on structural models is then approached at a later stage.

Here, we propose the direct fitting of the complete ED experimental pattern, where the simulated ED curve is built up using both the multiple scattering ED calculation and the *ISO* function, so that  $ED_{sim} = ISO(1 + \chi_{sim})$ . In Fig. 5 we present an example of full fit to a polar scan taken on the Fe Auger LMM line, for a 36 Å Fe film on Cu<sub>3</sub>Au(001). The data are presented as a function of the analyzer  $B$  angle (the normal emission direction, i.e. the zero for the polar angle  $\theta$ , is indicated by the vertical line). The  $\chi_{sim}$  component was calculated for a structural model by assuming the lateral lattice constant  $a = 2.830 \text{ \AA}$ , as measured by in-plane X-ray diffraction [8], and the vertical parameter  $c$  to be determined by the fitting procedure. The  $ED_{sim}$  was fitted to the experimental  $ED_{exp}$ , using in this case the roughness parameter  $\delta$  and the X-ray beam width  $\Gamma$  as fitting parameters. The layer thickness  $D$  was set to the value provided by the X-ray reflectivity calibration. In fact, being  $D$  already as large as  $3\lambda_{IMFP}$ , it would have yielded a contribution very similar to the  $D/\lambda \rightarrow \infty$  limit, strongly reducing the reliability of its determination by the minimization of the ED fitting procedure. An additional scale factor was also added to  $\chi_{sim}$  to take into account the ratio between the  $\chi$  and *ISO* amplitudes.

This procedure was iterated over a series of ED calculations, so that for each structure-dependent  $\chi_{sim}$ , the corresponding best fit *ISO* parameters can be found, thus eliminating any arbitrary *a priori* choice of the *ISO* shape. The best fit parameters of the *ISO* component were found to be  $\delta = 0.9 \pm 0.1$  and  $\Gamma = 160 \pm 20 \mu\text{m}$ .

Three additional curves are added in the Figure, as obtained by calculating the *ISO* component including only one factor each time. As anticipated before, the contribution due to the electrons escape depth is very close to the limit  $I_{IMFP} \sim \cos\theta$ . At low emission angles, the *ISO* shape is strongly affected by the illumination and roughness factors. The cross-section contribution is not shown, since the Auger emission was assumed to be isotropic. In fact, an exact calculation would have required a detailed study of all the decay channels participating to the Auger process [17], but the dependence on the angular momenta of the decay channels decreases as the kinetic energy increases, so that it becomes almost negligible at the present value of 698 eV [18].

At the bottom of Fig.5,  $\chi_{exp} = (ED_{exp} - ISO)/ISO$  and  $\chi_{sim} = (ED_{sim} - ISO)/ISO$  are compared to highlight the quality of the fit. With the given lateral lattice spacing  $a = 2.830 \text{ \AA}$ , we found the ratio of the vertical to lateral spacing to be  $c/a = 1.03 \pm 0.02$ . The Fe film displays a structure very close to its bcc bulk one,  $a = 2.86 \text{ \AA}$  and  $c/a = 1$ , the latter being recovered at a much higher thickness [19]. In general, this approach to the calculation of the *ISO* component leads to a substantial improvement of the reliability of the structural model (with an indetermination not exceeding a few percents).

## V. APPENDIX

The accurate description of the portion of illuminated area, which is included in the projected area of the analyzer slits onto the sample surface, is derived here for a generic scattering setup  $(B, C, \xi, \alpha)$ . For the sake of clarity, we will assume  $\xi = 0^\circ$ , since only the mutual orientation of  $\xi$  and  $C$  is relevant.

First, the orientation of the slits in the laboratory reference system is defined by the vectors  $\vec{B}_{slit}$  and  $\vec{C}_{slit}$  which connect the center of the slit with the center of the short and the long sides of the slits, respectively. The  $B$  and  $C$  labels recall that the wide aperture is along the direction scanned by the  $B$  angle, while the narrow one corresponds to a movement of the  $C$  rotation.

$$\vec{B}_{slit} = \frac{\Delta B}{2} \hat{k} \times \hat{B}_{axis} = \frac{\Delta B}{2} (\sin B, -\cos B \cos C, -\cos B \sin C) \quad (7)$$

$$\vec{C}_{slit} = \frac{\Delta C}{2} \hat{k} \times \hat{B}_{slit} = \frac{\Delta C}{2} (0, \sin C, \cos C), \quad (8)$$

where  $\hat{k} = (\cos B, \sin B \cos C, \sin B \sin C)$  is the photoelectron wavevector,  $\hat{B}_{axis} = (0, -\sin C, \cos C)$  is the orientation of the  $B$  rotation axis and  $\Delta B$  and  $\Delta C$  are the full slit aperture in the two directions.

The displacement of the four vertices of the slit from the center of the slit in the laboratory reference system is then

$$\vec{V}_j = \pm \vec{B}_{slit} \pm \vec{C}_{slit}; j = 1, 2, 3, 4. \quad (9)$$

The projection of the slit on the sample surface is in general a parallelogram, whose vertices are in the following positions in the laboratory reference system

$$\vec{S}_j = -\frac{\hat{n} \cdot \vec{V}_j}{\hat{n} \cdot \hat{k}} \hat{k} + \vec{V}_j, \quad (10)$$

where  $\hat{n}$  is the surface normal wavevector. The corresponding  $\vec{S}'_j$  positions in the (2-Dimensional) surface reference system are

$$\vec{S}'_j = (\vec{S}_j \cdot \hat{x}_{tilt}, \vec{S}_j \cdot \hat{y}_{tilt}), \quad (11)$$

$$\hat{x}_{tilt} = (\cos \alpha, 0, \sin \alpha), \quad (12)$$

$$\hat{y}_{tilt} = \hat{y}_{Lab}. \quad (13)$$

The width  $L(B, C, \alpha)$  of the portion of illuminated area falling inside the parallelogram can be computed as the minimum among the

$$L_j = 2 \left| \frac{\vec{S}'_{j+1,x} - \vec{S}'_{j,x}}{\vec{S}'_{j,y} - \vec{S}'_{j+1,y}} \vec{S}'_{j,y} + \vec{S}'_{j,x} \right|; j = 1, 2, 3, 4; \quad (14)$$

which are the crossing points of the parallelogram sides with the  $y = 0$  plane on the surface (we recall that the X-ray spot on the sample can be considered as monodimensional). The integration length on the surface may be further limited by the surface physical length.

- [1] J. Cooper and R.N. Zare, *J. Chem. Phys.* **48** (1968) 942.
- [2] C.S. Fadley, R.J. Baird, W. Siekhaus, T. Novakov, S.Å.L. Bergström, *J. Elect. Spectrosc. Relat. Phenom.* **4** (1974) 93-137.
- [3] C.S. Fadley, *The Study of Surface Structures by Photoelectron Diffraction and Auger Electron Diffraction in Synchrotron Radiation research: Advances in Surface and Interface Science, Vol. 1: Techniques*, edited by R. Z. Bachrach, Plenum Press, New York, (1992), and references therein.
- [4] D.P. Woodruff, *J. Electron Spectrosc. Relat. Phenom.* **100** (1999) 259-272.
- [5] MSCD is freely distributed by Y. Chen and M.A. Van Hove at: “<http://electron.lbl.gov/mscdpack/mscdpack.html>”; also see Y. Chen *et al.*, *Phys. Rev. B* **58** (1998) 13121.

- [6] M.-T. Lin, J. Shen, W. Kuch, H. Jenniches, M. Klaua, C.M. Schneider and J. Kirschner, Phys. Rev. B **55** (1997) 5886; Surf. Sci. **410** (1998) 298.
- [7] B. Schirmer, B. Feldmann and M. Wuttig, Phys. Rev. B **58** (1998) 4984.
- [8] F. Bruno, S. Terreni, L. Floreano, D. Cvetko, P. Luches, L. Mattera, A. Morgante, R. Moroni, A. Verdini, and M. Canepa, to be published, cond-mat/0103458.
- [9] L. Floreano, G. Naletto, D. Cvetko, R. Gotter, M. Malvezzi, L. Marassi, A. Morgante, A. Santaniello, A. Verdini, F. Tommasini and G. Tondello, Rev. Sci. Instrum. **70** (1999) 3855.
- [10] R. Gotter, A. Ruocco, A. Morgante, D. Cvetko, L. Floreano, F. Tommasini, and G. Stefani, Nucl. Instrum. Methods A **467-468** (2001) 1468.
- [11] Details of the experimental chamber can be found at the web page [www.tasc.infm.it/tasc/lds/aloisa/aloisa.html](http://www.tasc.infm.it/tasc/lds/aloisa/aloisa.html).
- [12] J. Wider, F. Baumberger, M. Sambì, R. Gotter, A. Verdini, F. Bruno, D. Cvetko, A. Morgante, T. Greber and J. Osterwalder, Phys. Rev. Lett. **86** (2001) 2337.
- [13] A. Verdini, M. Sambì, F. Bruno, D. Cvetko, M. Della Negra, R. Gotter, L. Floreano, A. Morgante, G.A. Rizzi, G. Granozzi, Surf. Rev. Lett. **6** (1999) 1201.
- [14] J. J. Yeh, *Atomic Calculation of Photoionization Cross-Sections and Asymmetry Parameters*, Gordon and Breach Science Publ. (1993).
- [15] S. Tanuma, C.J. Powell, D.R. Penn, Surf. Interface Anal. **20** (1993) 77.
- [16] A.V. Yakovenko, J. Electron Spectrosc. Relat. Phenom. **74** (1995) 237-240.
- [17] T. Greber, J. Osterwalder, D. Naumovic, A. Stuck, S. Hüfner, and L. Schlapbach, Phys. rev. Lett. **69** (1992) 1947.
- [18] Y.U. Ydzerda, Surf. Rev. Lett. **4** (1997) 161.
- [19] R. Rocow, C. Carbone, Th. Dodt, F.P. Johnen and E. Kisker, Phys. Rev. B **41** (1990) 3426.

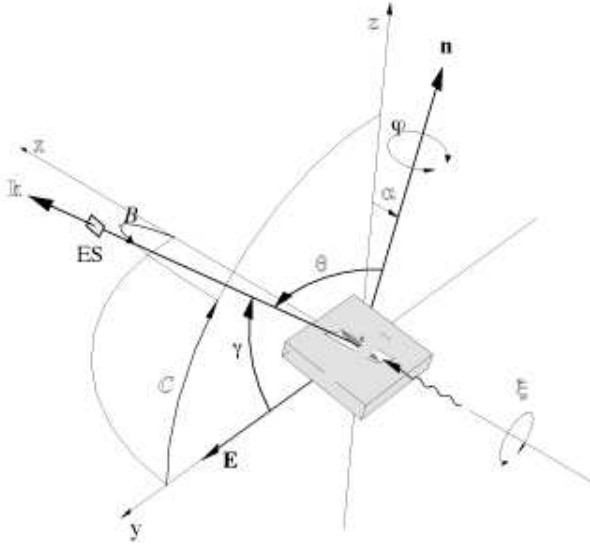


FIG. 1. Degrees of freedom in the choice of the scattering geometry for the ALOISA experimental station. The rotating electron analyzer is represented by its entrance slits  $ES$ ; the projection of the slits onto the sample surface is drawn as a white parallelogram, defining the portion of surface contributing to the electron yield. The X-ray beam footprint on the surface (illuminated area) is shown as a shadowed ellipsis. The manipulator rotations  $\alpha$ ,  $\phi$  and  $\xi$  are used to select independently the grazing angle, the azimuthal orientation and the orientation of the surface with respect to the beam polarization vector  $\vec{E}$ . The analyzer rotations  $B$  and  $C$  allows one to survey most of the sky over the sample surface. The polar angle  $\theta$  (emission angle referred to the surface normal  $\hat{n}$ ) and the  $\gamma$  angle (between the photoelectron wavevector  $\vec{k}$  and  $\vec{E}$ ) are also shown.

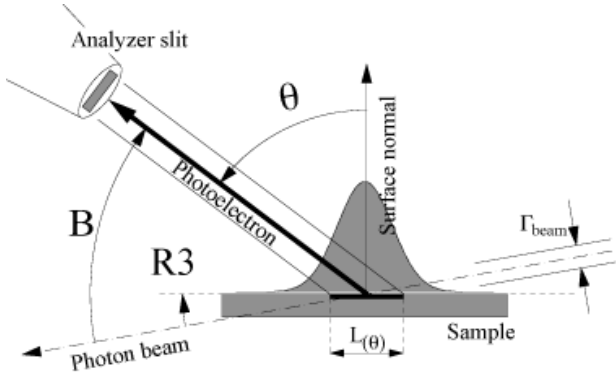


FIG. 2. Schematic model of the intensity distribution of the photon beam illuminated area on the sample surface, for polar scans taken rotating the analyzer in the scattering plane. The projection of the analyzer slit on the surface  $L(\theta) = \Delta / \cos \theta$  provides the integration limits in Eq. 5.

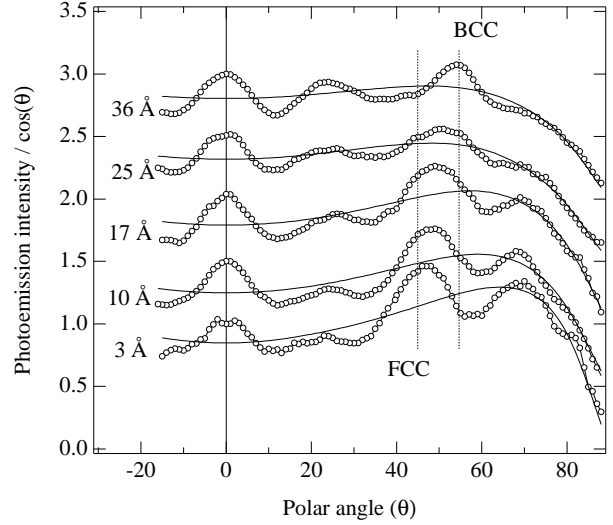


FIG. 3. Polar scans taken for the Fe Auger LMM line from a growing crystalline Fe overlayer on  $\text{Cu}_3\text{Au}(001)$ . The thickness dependence of the ISO distribution, also shown in the picture, has been highlighted by dividing both the data and the ISO curves by  $\cos \theta$ . The thicknesses have been independently determined by x-ray reflectivity.

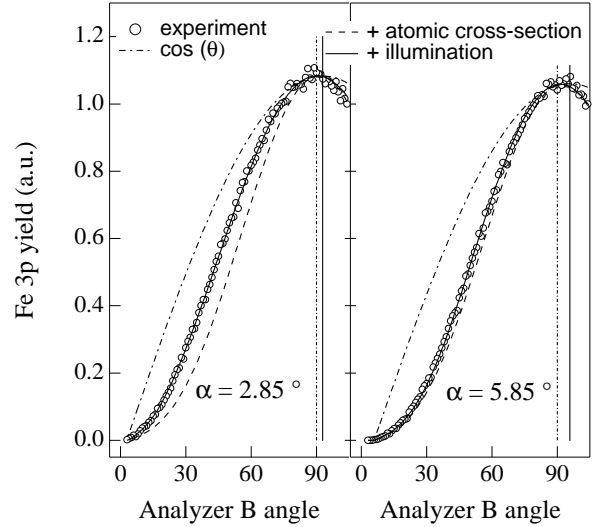


FIG. 4. Polar scans of Fe 3p intensity (at a kinetic energy of 803 eV) from the surface of a polycrystalline Fe sample are compared with calculated ISO functions, built by successive inclusion of the different factors (with  $\beta=1.485$  for the atomic cross section factor and  $\Gamma_{beam}=150 \mu\text{m}$  for the illumination factor). The full ISO function fits the experimental data with the same set of parameters (see text) for both the scans, taken at different value of grazing angle  $\alpha$ . The vertical full line indicates the surface normal direction, while the vertical dot-dashed line is the direction of the photon beam electric field.

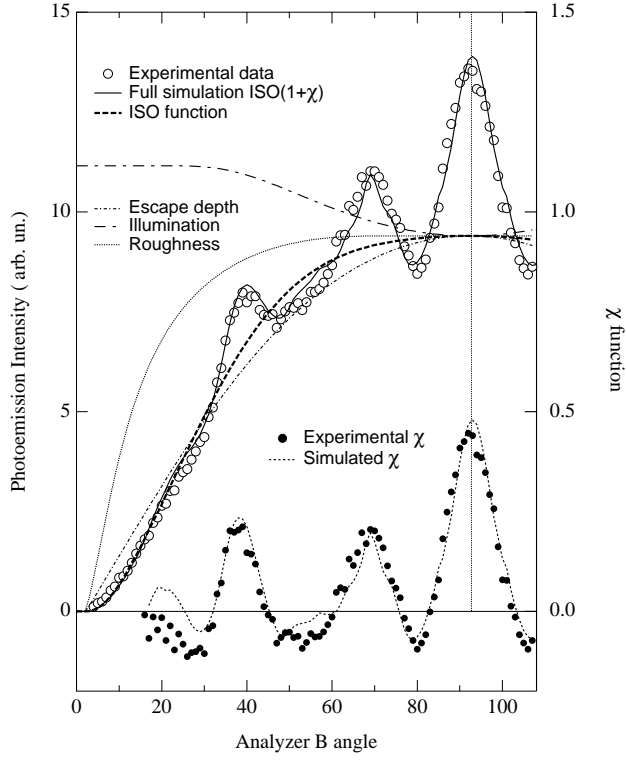


FIG. 5. Fe Auger LMM polar scan taken for the 36 Å Fe film on Cu<sub>3</sub>Au(001). The experimental ED pattern is shown together with the full simulation  $ED_{sim}$  and the corresponding  $ISO$  function. At the bottom,  $\chi_{exp} = (ED_{exp} - ISO)/ISO$  and  $\chi_{sim} = (ED_{sim} - ISO)/ISO$  are compared. Three additional curves are added, as obtained recalculating the  $ISO$  including only one factor at a time. The cross-section contribution is not shown, since we approximated the Auger emission with an isotropic distribution. The normal emission direction is indicated by the vertical line.